BNL-224904-2023-TECH

EIC-ADD-TN-055

Eddy Current Shielding of the Magnetic Field Ripple in the EIC Electron Storage Ring Vacuum Chambers

B. Podobedov

September 2023

Electron-Ion Collider

Brookhaven National Laboratory

U.S. Department of Energy

USDOE Office of Science (SC), Nuclear Physics (NP) (SC-26)

DISCLAIMER

Eddy Current Shielding of the Magnetic Field Ripple in the EIC Electron Storage Ring Vacuum Chambers

Boris Podobedov, Michael Blaskiewicz

Brookhaven National Laboratory, Upton, NY, 11733, USA

(Dated: September 30, 2023)

I. INTRODUCTION

The EIC electron storage ring (ESR) has very tight tolerances for the beam position and size stability at the interaction point. The oscillations at the proton betatron frequency and its harmonics are the most dangerous because, for instance, they could lead to unacceptable proton emittance growth from the oscillating beam-beam kick from the electrons at the amplitude of the positional oscillations as low as 10^{-4} of the beam size [1]. Even at much lower frequencies, down to the single Hz range, the position oscillations at a few percent level of the nominal beam size were found to be dangerous [2].

These oscillations could have different causes including magnet power supply ripple, magnet vibration, noise in the main and crab RF systems, and some collective instabilities. To specify the acceptable level of the current ripple and noise of the magnet power supplies we need to accurately account for the eddy current shielding by the vacuum chamber, as well as, potentially, by the laminated magnet yokes (considered elsewhere). With some approximations, the chamber shielding can be described analytically. The main objective of this note is to derive these analytical expressions and to document the resulting shielding performance of the ESR chamber. The implications of this shielding for the power supply ripple specifications are presented in [3].

The dipole and multipole chambers in the ESR have elliptical cross-sections with 4-mm thick copper walls, with some protrusions on the sides, see Fig. 1. At frequencies above approximately 300 Hz, the skin depth becomes smaller than the wall thickness. This results in the well-known single-pole expressions for the eddy current shielding transfer function (reviewed in Section II) greatly underestimating the shielding effect, especially at higher frequencies. In this note, we present analytical formulas that adequately describe this shielding at any relevant frequency and for magnetic multipoles of arbitrary order. For simplicity, we approximate the chamber by an axially symmetric geometry which is conservative and adequate for the power supply ripple specifications.

The penetration of a time-varying magnetic field inside a long tubular cylinder can be described by standard methods of classical electrodynamics. The treatment is further simplified at low frequencies, where the displacement currents can be ignored, and the quasistatic approximation can be used. Equivalent expressions for the shielding of the dipole field have been published earlier. However, to the best of our knowledge, the shielding expressions

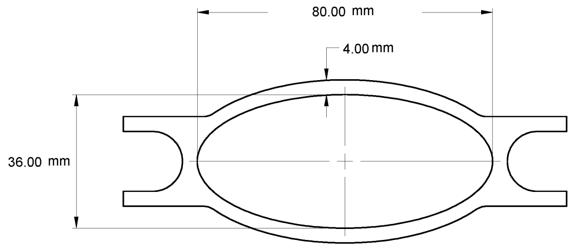

FIG. 1. ESR vacuum chamber cross-section (courtesy Charles Hetzel).

for higher-order multipoles (quadrupole, sextupole, etc.) have not been published, making these results new. Additionally, we will present the rational expansions of the field transfer functions in terms of a small number of poles, which are intuitive and practical for use.

The rest of this note is structured as follows. In Section II, we review the standard expressions for the eddy current shielding due to a thin-wall vacuum chamber. In Section III, we derive the shielding expressions (or, more generally, the transfer functions) for arbitrary order magnetic multipoles and valid for arbitrary ratios of the skin depth to the wall thickness. In Section IV, we discuss some physics aspects of these transfer functions and present their rational function approximations. In Section V we provide a brief summary of our findings and their implications for the ESR. Finally, for reference purposes, the field attenuation values for the ESR vacuum chambers at the harmonics of 60 Hz power-line frequency below 1 kHz are tabulated in the Appendix.

II. THIN-WALL EXPRESSIONS

Time-varying external magnetic fields are attenuated and delayed inside the vacuum chamber due to the induced eddy currents that flow along the chamber wall. The effect is the simplest when the current variation over the wall thickness due to the skin effect can be neglected (electrically thin wall or weak skin effect approximation). Then, for a non-magnetic (μ_r=1) beam pipe with a circular cross-section with radius r_0, thickness d, and conductivity σ, subjected to a varying external dipole field, $B_e(t) = B_0 \sin(\omega t)$, the field inside is [4], [5]

$$B_i(t) = \frac{B_0}{\sqrt{1+\omega^2\tau^2}} \sin(\omega t - \tan^{-1}(\omega\tau)), \tag{1}$$

with the time constant given by

$$\tau = \frac{1}{2}\mu_0 \sigma r_0 d, \tag{2}$$

and μ_0 denoting the permeability of free space.

Eq. (1) corresponds to the steady-state response of a 1st-order dynamical system with the Laplace-domain ($p = j\omega$) transfer function

$$H_{dipole}(p) = \frac{\tilde{B}_i(p)}{\tilde{B}_e(p)} = \frac{1}{1 + p\tau}, \tag{3}$$

which has a single pole at $p = p_0 = -1/\tau$. At frequencies $\omega \gg 1/\tau$ the field attenuation is 20 dB/decade and the phase inside the chamber lags by $\pi/2$.

Eq. (3) can be generalized to higher-order transverse multipole fields (see [4], [5]). Below we use the standard multipole expansion in polar coordinates $\{r, \theta\}$ for the external field scalar potential,

$$\mathbf{B}_e(r, \theta) = \nabla \Phi_e, \tag{4}$$

$$\Phi_e = \sum_{m=1}^{\infty} r^m (a_{m,e} \cos m\theta + b_{m,e} \sin m\theta). \tag{5}$$

Here $\tilde{b}_m$ and $\tilde{a}_m$ are the regular and skew multipole coefficients respectively, and the indices m=1,2,3,... correspond to the dipole, quadrupole, sextupole, etc.

We now assume that the external field contains only one regular multipole of order m, which is harmonically time-varying, i.e. $b_{m,e} \propto \sin \omega t$. The transfer function for the field inside the chamber relative to that without the chamber (i.e. when the field everywhere equals $\mathbf{B}_e(r, \theta)$) can be written as

$$H_m(p) = \frac{\tilde{b}_{m,i}(p)}{\tilde{b}_{m,e}(p)} = \frac{1}{1 + p\tau/m}. \tag{6}$$

The transfer function for the skew fields is identical due to symmetry. Eqs. (6) implies that for higher-order multipoles the attenuation becomes significant at a proportionally higher frequency, e.g. a factor of two attenuation occurs at $\omega_{6\mathrm{dB}} = m/\tau$.

The time-domain equivalent of Eq. (6) for the normal multipole component, assuming $b_{m,e}(t) = b^0_{m,e} \sin \omega t$, is

$$b_{m,i}(t) = \frac{b^0_{m,e}}{\sqrt{1 + (\omega\tau/m)^2}} \sin(\omega t - \tan^{-1}(\omega\tau/m)), \tag{7}$$

and the same expression holds for the skew component.

Eqs. (6)-(7) can be derived assuming that a particular multipole symmetry holds to $r = \infty$, where the undisturbed external field is taken for the boundary condition[1],

$$\mathbf{B}(r,\theta)|_{r\to\infty} = \nabla\big(r^m b_{m,e} \sin m\theta\big). \tag{8}$$

This results in the transfer functions due to different orders m being fully uncoupled.

In reality, the apertures of accelerator magnets are finite and they do not present magnetic boundary conditions that correspond to a pure single multipole. Therefore, even in the case of a circular chamber, the boundary conditions at the magnet make complete separation of the multipole field harmonics not generally achievable.

For instance, a more accurate boundary condition due to high-permeability steel poles used in typical C- or H- dipole magnets, requires $\vec{B}$ to be normal to the pole faces, which can be modeled by two parallel infinitely permeable plates, separated by the magnet gap g. As S.Y. Lee has shown in [6], this boundary condition modifies the eddy currents induced in the chamber wall, making them not only attenuate the AC-varying external dipole field but also create small sextupole and other higher-order field harmonics even for an axially-symmetric vacuum chamber. While these dynamic multipoles (or the ones caused by the asymmetric chambers) could be important for the lattice design of ramping machines, such as the EIC RCS, they can be neglected for the beam pipe shielding estimates due to the magnet current ripple performed here.

Another consequence of these more nuanced boundary conditions in the dipole, which can be seen from Eq. (16) of [6], applied to a circular chamber, is that the shielding time constant becomes a factor of $(1 + \frac{\pi^2}{3}(r_0/g)^2)$ longer compared to Eq. (2). (Of course, the time constants agree, when $g \gg r_0$.) For simplicity, we will ignore this effect below as well and adhere to the simpler boundary conditions at infinity, while acknowledging that this will result in our subsequent estimates being more conservative.

III. SHIELDING OF MULTIPOLE FIELDS AT ARBITRARY WALL THICKNESS

In this section, we assume that the chamber is an infinite cylinder along z direction with the inner and outer radii given by a and b, as shown in Fig. (2). We start with the relevant

---

[1] Equivalently, one can assume that B_e is created by an ideal "Cosine-theta" coil with the radius $r_1 > r_0$, and fix the outer boundary condition at $r = r_1$ [4].

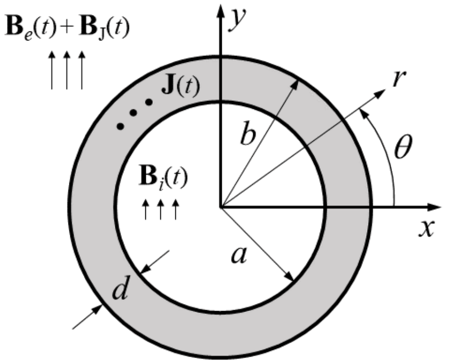

FIG. 2. Notation and coordinate system; z-axis points out of the page. B-fields are purely transverse. $\mathbf{B}_i(t)$ is the field inside the chamber. Outside the chamber, the field is a sum of the externally applied field, $\mathbf{B}_e(t)$, and the induced $\mathbf{B}_\mathrm{J}(t)$, due to eddy currents $\mathbf{J}(t) = J_z(t)\hat{\mathbf{z}}$ in the pipe wall.

Maxwell's equations in the quasistatic approximation (valid due to the geometric dimensions in the problem being much smaller than the wavelengths of the electromagnetic wave at the frequencies of interest),

$$\nabla \times \mathbf{E} = -\frac{\partial \mathbf{B}}{\partial t}, \tag{9}$$

$$\nabla \times \mathbf{B} = \mu_0 \mathbf{J}. \tag{10}$$

Expressing the magnetic field, $\mathbf{B} = \nabla \times \mathbf{A}$, in terms of the vector potential $\mathbf{A}$, and setting $\mathbf{J} = \sigma \mathbf{E}$ inside the chamber wall, we get

$$\nabla^2 \mathbf{A} = -\mu_0 \sigma \mathbf{E}, \quad a \le r \le b. \tag{11}$$

In the free space inside and outside the chamber the potential satisfies the Laplace equation.

From translational symmetry and $\mathbf{B}$ being purely transverse, $\mathbf{E}$, $\mathbf{J}$, and $\mathbf{A}$ are directed along the chamber, in z-direction.

Combining the equations above, we can write for $A \equiv A_z$, in cylindrical coordinates,

$$\nabla^2 A = \frac{1}{r}\frac{\partial}{\partial r}\left(r\frac{\partial A}{\partial r}\right) + \frac{1}{r^2}\frac{\partial^2 A}{\partial \theta^2} = \mu_0 \sigma \frac{\partial A}{\partial t}, \quad a \le r \le b. \tag{12}$$

We now separate the multipolar fields assuming harmonic θ-dependence for the vector potential. The equivalent of Eq. (5), written for the z-component of the vector potential of the external driving field, is

$$A_e = \sum_{m=1}^{\infty} r^m (a_{m,e} \sin m\theta - b_{m,e} \cos m\theta). \tag{13}$$

From here we will only carry the regular (b_m) component. Separating the multipoles and noting that the azimuthal variation should be the same everywhere in space due to symmetry, we factor out the r-dependence,

$$A_m(r,\theta,t) = u_m(r,t)\cos m\theta. \tag{14}$$

Outside the pipe wall, the radial function, which matches the external driving field $\mathbf{B}_e$ at infinity, is then

$$u_m(r,t) = b_{m,i}(t)r^m, \quad r < a \tag{15}$$

$$u_m(r,t) = f(t)r^{-m} + b_{m,e}(t)r^m, \quad r > b, \tag{16}$$

or, in the Laplace domain,

$$\tilde{u}_m(r,p) = \tilde{b}_{m,i}(p)r^m, \quad r < a \tag{17}$$

$$\tilde{u}_m(r,p) = \tilde{f}(p)r^{-m} + \tilde{b}_{m,e}(p)r^m, \quad r > b. \tag{18}$$

We assume that the coefficient $b_{m,e}$ is known, while $b_{m,i}$ and the function f are to be found.

Plugging Eq. (14) into Eq. (12) and performing the Laplace transform we get

$$\frac{\partial^2\, \tilde{u}_m(r,p)}{\partial r^2} + r\frac{\partial\, \tilde{u}_m(r,p)}{\partial r} - \left(q^2 + \frac{m^2}{r^2}\right)\tilde{u}_m(r,p) = 0, \quad a \le r \le b, \tag{19}$$

where we introduced

$$q = (\mu_0 \sigma p)^{\frac{1}{2}}. \tag{20}$$

Eq. (19) must be solved with the boundary conditions of continuity of the tangential ($B_\theta = -\frac{\partial A}{\partial r}$) and normal ($B_r = \frac{1}{r}\frac{\partial A}{\partial \theta}$) components of the magnetic field at $r = a$ and $r = b$. These conditions at each boundary can be combined to eliminate $\tilde{b}_{m,i}(p)$, and written as

$$m\, \tilde{u}_m(a,p) - a\, \frac{\partial \tilde{u}_m(r,p)}{\partial r}\bigg|_{r=a} = 0, \tag{21}$$

$$2\, m\, b^m \tilde{b}_{m,e}(p) + m\, \tilde{u}_m(b,p) + b\, \frac{\partial \tilde{u}_m(r,p)}{\partial r}\bigg|_{r=b} = 0. \tag{22}$$

With these boundary conditions, the solution of Eq. (19) is

$$\tilde{u}_m(r,p) = \frac{2mb^{m-1}}{q}\frac{I_{m+1}(aq)K_m(qr) + K_{m+1}(aq)I_m(qr)}{I_{m+1}(aq)K_{m-1}(bq) - K_{m+1}(aq)I_{m-1}(bq)}\tilde{b}_{m,e}(p), \quad a \le r \le b, \tag{23}$$

where $I_m(...)$ and $K_m(...)$ stand for the modified Bessel functions of order m.

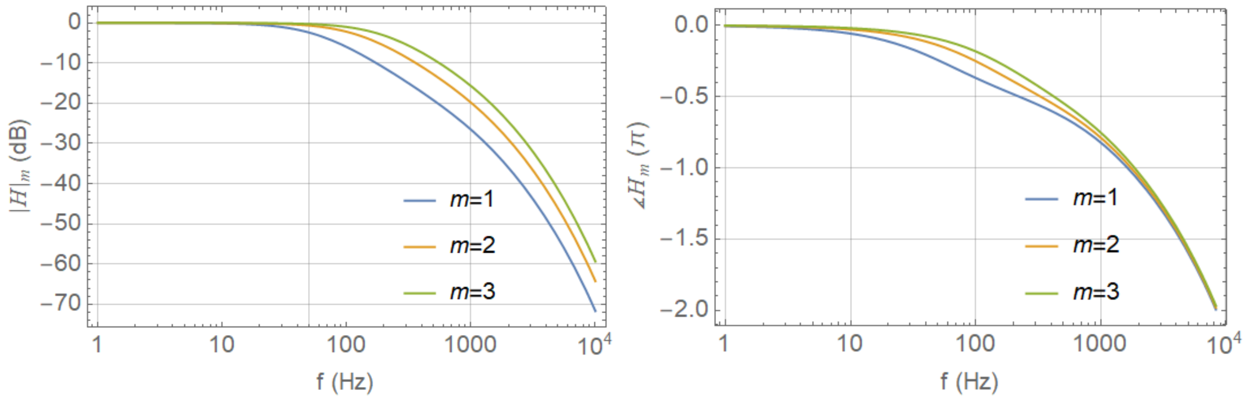

FIG. 3. Attenuation and phase lag of the external dipole, quadrupole, and sextupole magnetic field inside the beam pipe.

Dividing this solution, taken at $r = a$, by $\tilde{b}_{m,e}(p)\, a^m$, we obtain the transfer function, $\tilde{b}_{m,i}(p)/\tilde{b}_{m,e}(p)$. The final result is

$$H_m(p) = \frac{2\, m\, \left(\frac{b}{a}\right)^m}{a\, b\, q^2 \big(K_{m+1}(a\, q) I_{m-1}(b\, q) - I_{m+1}(a\, q) K_{m-1}(b\, q)\big)}, \tag{24}$$

where the p-dependence enters through $q = q(p)$, as defined in Eq. (20). It is worth pointing out that the absolute values of the arguments of the Bessel functions are $\sqrt{2}$ times the ratio of the corresponding radius to the skin depth,

$$|a\, q| = \sqrt{2}\; a/\delta_{sk}, \text{ (same for } b), \tag{25}$$

$$\delta_{sk} = \delta_{sk}(\omega) = \sqrt{\frac{2}{\mu_0 \sigma \omega}}. \tag{26}$$

Equivalent expressions to Eq. (24) for the dipole field (m=1) transfer function can be found in literature, see e.g. [7]-[10]. These include much bulkier formulas for the case of magnetic wall material, $\mu_r > 1$. However, as stated in the Introduction, we are not aware of any published expressions for $m > 1$, so Eq. (24) should be considered new.

In Fig. (3) we plot the amplitude and phase of the transfer function from Eq. (24) for the three lowest multipoles, using the relevant ESR chamber parameters. (Also, for reference purposes, the field attenuation values for the ESR vacuum chambers at the harmonics of 60 Hz power-line frequency below 1 kHz are tabulated in the Appendix.)

For this figure, and throughout the rest of the paper, we assume a copper pipe with d=4 mm wall thickness and use the values a=18 mm, b=22 mm, and σ=5.8×10^7 $(\Omega \times \mathrm{m})^{-1}$. We took the smallest dimensions of the actual chamber cross-section for the radii (the half-heights in Fig. 1), so that our shielding estimates remain conservative. With these parameters, the numerical value for the time constant is $\tau = 2.62$ ms.

At low frequency, the response seen in Fig. 3 agrees with that due to a thin-wall pipe, Eq. (6). However, the high-frequency response is showing significant deviation. The slope of attenuation with frequency keeps increasing beyond 20 dB/decade. The phase lag also increases with accelerating slope, greatly surpassing the $\pi/2$ high-frequency limit of Eq. (6). This will be discussed further in the next section.

Meanwhile, we briefly discuss a related effect, i.e. the distribution of eddy currents, $J = -\sigma\frac{\partial A}{\partial t}$, inside the pipe wall. The azimuthal distribution is $\propto \cos m\theta$, while the r-dependence is captured in the numerator of Eq. (23),

$$\tilde{u}_m(r,p) \propto I_{m+1}(aq)K_m(qr) + K_{m+1}(aq)I_m(qr), \quad a \le r \le b. \tag{27}$$

The absolute value of this expression is monotonically rising with r, reaching maximum at $r = b$, where the induced current is the strongest. As follows from the asymptotic properties of the Bessel functions, at low-frequency, this rise is linear and very gradual, while at high-frequency the rise is exponential and occurs mainly near $r = b$. In other words, at higher frequencies, the eddy currents are concentrating closer to the outer pipe radius, decreasing the effective conducting wall thickness and lengthening the time constant.

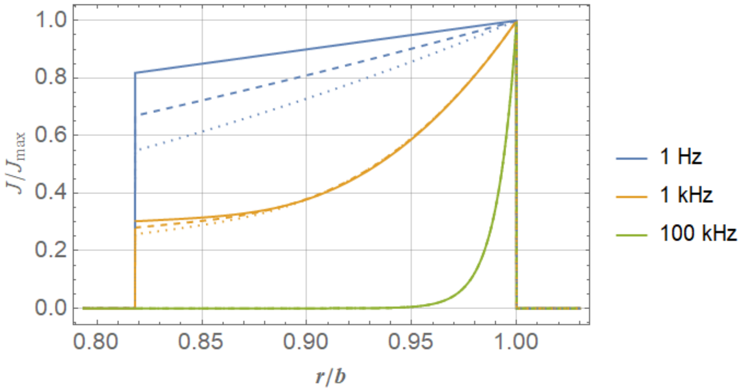

FIG. 4. Radial distribution of eddy currents inside the pipe wall for the dipole (solid), quadrupole (dashed), and sextupole (dotted) excitation.

This is illustrated in Fig. (4) where we plot the radial dependence of the current density normalized to its maximum value at $r = b$. The difference between the multipoles is relatively minor at low frequencies and it disappears at high frequencies, where the current dies off a few skin depths away from the outer surface. For reference, the ESR chamber skin depth at 100 kHz is 0.2 mm or 1% of b, which is consistent with the green curves in the figure.

IV. APPROXIMATION OF THE SHIELDING TRANSFER FUNCTION

Here we further analyze the transfer function $H_m(p)$ given by Eq. (24), with the goal of getting a better understanding, as well as coming up with some simplifying approximations, including for axially asymmetric chambers.

The poles of the transfer function are the roots of the equation,

$$a\,b\,q^2\big(K_{m+1}(a\,q)I_{m-1}(b\,q) - I_{m+1}(a\,q)K_{m-1}(b\,q)\big) = 0. \tag{28}$$

We now define the time constant for the pipe as (cf. Eq. (2))

$$\tau = \frac{1}{2}\mu_0 \sigma a d, \tag{29}$$

introduce the normalized wall thickness by

$$\kappa = d/a, \tag{30}$$

and switch to a unitless variable

$$u = a\,q = (2p\tau/\kappa)^{1/2}. \tag{31}$$

Eq. (28) becomes

$$u^2(1+\kappa)\big(K_{m+1}(u)I_{m-1}(u+\kappa\,u) - I_{m+1}(u)K_{m-1}(u+\kappa\,u)\big) = 0. \tag{32}$$

The root with the smallest absolute value corresponds to the dominant pole p_0 of the transfer function $H_m(p)$. It is easily found by Taylor-expanding the Bessel functions in Eq. (32) to the leading order in $\kappa\,u$. From Eq. (25), the physical meaning of $|\kappa\,u|$ is $\sqrt{2}$ times the ratio of the wall thickness to the skin depth. Therefore, this expansion results in a good approximation of the transfer function when $\delta_{sk} \gg d$.

Ignoring small corrections on the order of $O[\kappa]$, the solution to the resulting linear equation in p is then

$$p_0 = -m/\tau, \tag{33}$$

which agrees with the thin-wall transfer function, Eq. (6).

The rest of the roots of Eq. (32) must occur at large values of the Bessel function arguments, where the well-known asymptotic approximations apply, i.e. $I_m(ix) \propto \cos{(x + \frac{\pi}{4} + \frac{m\pi}{2})}/\sqrt{x}$ and $K_m(ix) \propto (\cos x + i \sin x)/\sqrt{x}$. (The poles must be real and negative for stability, so we only need to consider purely imaginary values of Bessel's arguments). Sine and cosine functions result in an infinite number of easy-to-find distinct roots, corresponding to the poles of $H_m(p)$, which can be approximately written as

$$p_n = -n^2 \frac{\pi^2}{\mu_0 \sigma d^2}, \quad n = 1, 2, 3, ... \tag{34}$$

In contrast to p_0, these poles do not depend on the multipole order m, or the chamber radius, and they scale inversely with the square of the wall thickness.

It is easy to check that these poles correspond to frequencies where the skin depth is equal to $\frac{\sqrt{2}}{\pi}\, d/n$. Therefore, to adequately approximate the system response when the skin depth is comparable or smaller than the wall thickness, multiple of these poles are required. For example, for the ESR chamber at 10 kHz, the skin depth is 0.66 mm and much smaller than the wall thickness. This explains the difference, mentioned earlier, between the responses shown in Fig. (3) from the ones expected for a thin-wall chamber.

Separately, the fact that these "skin-effect poles" are independent of m, explains why, at high frequency, the attenuation curves in Fig. (3) become parallel to each other and the phase curves merge together.

With this understanding of the poles of the exact transfer function, we suggest a simple rational function approximation,

$$H_m(p) \approx \prod_{n=0}^{N-1} \frac{p_n}{p - p_n}, \tag{35}$$

where the poles p_n are given by Eqs.(33)-(34). The total number of poles N (and therefore the order of the corresponding linear dynamical system) can be chosen depending on the highest frequency of interest.

For our circular approximation of the ESR chamber cross-section, $|p_0|/2\pi$=60.66 Hz and $|p_{n>0}|/2\pi = n^2 \times 1347$ Hz. Using these values, several dominant pole approximations, together with the exact expression, Eq. (24), are plotted in Fig. 5. The convergence to the exact transfer function with increasing N is evident. Quantitatively, N=3 poles approximate the attenuation within 3 dB accuracy up to 10 kHz. For the phase, the N=8 approximation is accurate to better than a degree up to 1 kHz. On the other hand, the thin-wall approximations (N=1) are only accurate for the attenuation roughly below a kHz, and they greatly underestimate both the attenuation and phase lag at higher frequencies.

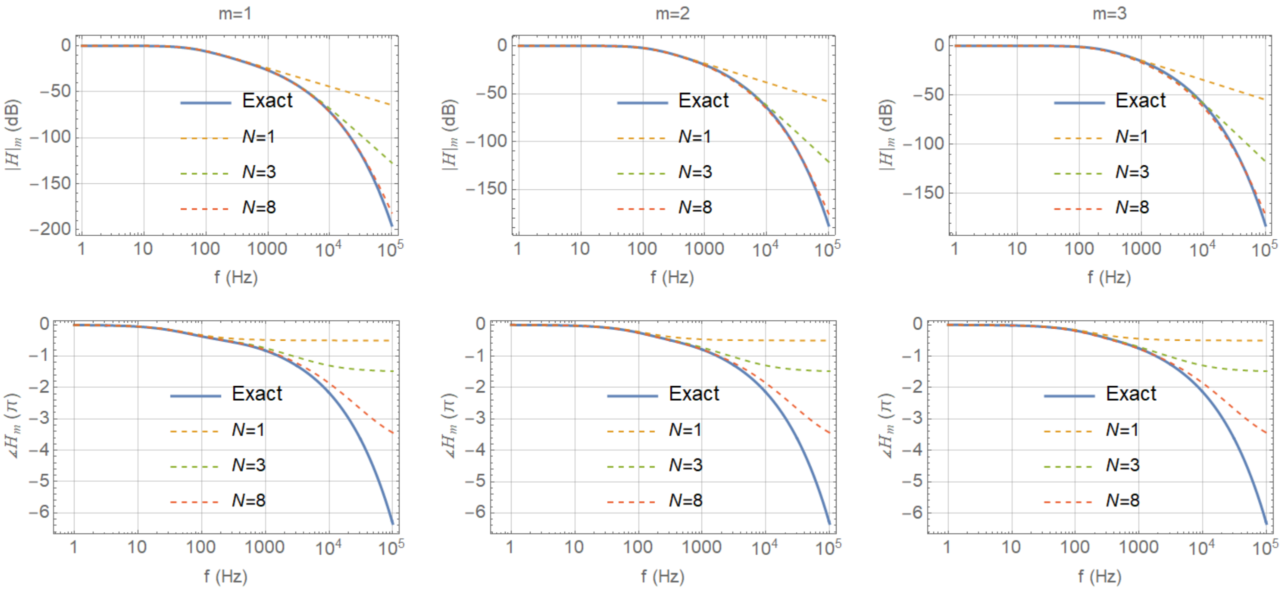

FIG. 5. Attenuation (top) and phase lag (bottom) of the external (left-to-right) dipole, quadrupole, and sextuple field inside the beam pipe from Eq. (24) (solid) and N=1-, 3-, and 8-pole approximations from Eq. (35) (dashed).

Finally, we mention that it is possible to extend the approximate transfer function, Eq. (35), to axially asymmetric chambers. This was first suggested in [11] for the dipole field and confirmed with numerical EM field calculations and magnetic measurements. Essentially the idea is to replace the dominant pole p_0 with the inverse of the thin-wall time constant for the asymmetric chamber. This time constant could be found by extending the approach of S.Y. Lee [6] or by other methods. Unlike the case of an axially symmetric chamber, this time constant depends on the external field orientation, so the resulting transfer functions for the normal and skew fields are different. Also, the simple scaling of the dominant pole with m, Eq. (33), is not applicable to asymmetric chambers.

On the other hand, the Eq. (35) poles p_n, with $n > 0$, should be approximately the same for an axially asymmetric chamber, as for a symmetric one. This is intuitively clear because the skin effect matters mostly when the skin depth is comparable to or smaller than the wall thickness, so the asymmetry between much larger dimensions of the chamber height and width does not affect these poles.

Approximating the ESR chamber by an ellipse with the aspect ratio of $80/36\approx 2.22$, we find from Eq. (6) of [11] that the dominant pole for the normal dipole shifts down to $|p_0|/2\pi$=29.52 Hz. For vertical dipole correctors (horizontal B-field) it becomes $|p_0|/2\pi$=47.22 Hz. These estimates suggest that the results of this note, obtained for the axially symmetric approximation of the ESR chamber, are conservative and accurate to within a factor of two.

V. SUMMARY AND DISCUSSION

We derived the transfer function which describes the penetration of time-varying magnetic fields with arbitrary multipole symmetry into a conductive non-magnetic vacuum chamber with a circular cross-section. Our main result, Eq. (24), applies for arbitrary ratios of the skin depth to the wall thickness. We also suggested an accurate and physically intuitive approximation of this transfer function, Eq. (35), which is simple and handy for most practical purposes, where a small number of poles is usually sufficient.

Numerical results for the ESR chamber shielding were documented in Figs. (3)-(5) as well as tabulated in the Appendix for a handful of power-line harmonics. We have also included the phase response results. While irrelevant for the shielding, the phase response is important for the design of feedback systems that use magnet correctors or main magnets as actuators.

The shielding by the ESR chamber was found to be very substantial at high frequencies, e.g. exceeding 70 dB for the dipole above 10 kHz. This argues that crediting just the chamber shielding is sufficient for the beam position and size oscillations, potentially caused by the magnet power supply ripple at the proton betatron frequency and its harmonics, because the resulting power supply specifications are not very restrictive, see [3] and [12] for more detail.

However, at frequencies below approximately 1 kHz, crediting the shielding provided by the chamber alone results in the dipole power supply current ripple specifications at or beyond the state-of-the-art, as discussed in [3]. (The specifications for the quadrupole and sextupole power supplies remain within comfortable limits.) Therefore, considering additional sources of shielding, such as eddy currents in the magnet yokes, or exploring alternative solutions to relax the dipole power supply ripple specifications may be necessary.

---

[1] M. Blaskiewicz, NAPAC'2019, TUPLM11

[2] D. Xu, M. Blaskiewicz, Y. Luo, D. Marx, C. Montag, B. Podobedov, IPAC'2023, MOPA039

[3] B. Podobedov, M. Blaskiewicz, Y. Luo, D. Marx, C. Montag, D. Xu, BNL-224464-2023-TECH, EIC-ADD-TN-059

[4] R.E. Shafer, Fermilab report TM-991 (1980)

[5] A.W. Chao, K.H. Mess, M. Tigner, F. Zimmermann, "Handbook of Accelerator Physics and Engineering", 2013, Edition 2, World Scientific, In Chap. 4, Section 4.5.1, D. Rice, "Error Sources and Effects".

[6] S.Y. Lee, NIM-A, 300 (1991), p. 151

[7] S. Celozzi, R. Araneo, G. Lovat, "Electromagnetic Shielding", John Wiley & Sons, Inc., 2008

[8] S. Fahy, C. Kittel, S. G. Louie, Am. J. Phys. 56, 989–992 (1988) https://doi.org/10.1119/1.15353

[9] W. R. Smythe, Static and Dynamic Electricity, 3rd ed., Hemisphere Pub. Corp., 1989

[10] S.H. Kim, APS note LS-291 (2001)

[11] B. Podobedov, L. Ecker, D. Harder, G. Rakowsky, PAC'09, TH5PFP083

[12] B. Podobedov, M. Blaskiewicz, Transversely Driven Coherent Beam Oscillations in the EIC Electron Storage Ring, EIC-ADD-TN-054, TBC

Appendix A: Chamber attenuation at the harmonics of power-line frequency

Magnetic field ripple attenuation in the ESR chamber calculated from Eq. (24) is given in the table below.

	Attenuation at powerline harmonic frequencies in dB															
	60 Hz	120 Hz	180 Hz	240 Hz	300 Hz	360 Hz	420 Hz	480 Hz	540 Hz	600 Hz	660 Hz	720 Hz	780 Hz	840 Hz	900 Hz	960 Hz
dipole	3.15	7.23	10.3	12.67	14.59	16.21	17.62	18.87	20.0	21.04	22.0	22.9	23.76	24.57	25.34	26.08
quad	0.92	2.90	4.98	6.87	8.52	9.98	11.28	12.46	13.53	14.52	15.44	16.31	17.13	17.91	18.65	19.37
sext	0.39	1.39	2.68	4.03	5.34	6.56	7.07	8.76	9.74	10.66	11.52	12.34	13.12	13.86	14.57	15.26